Available online at www.sciencedirect.com
SCIENCE DIRECT®
Earth and Planetary Science Letters 244 (2006) 458–473
EPSL
www.elsevier.com/locate/epsl

The rift to drift transition at non-volcanic margins: Insights from numerical modelling

Marta Pérez-Gussinyé [a,*], Jason Phipps Morgan [b,1], Timothy J. Reston [c], César R. Ranero [d,1]

[a] Institute of Earth Sciences "Jaume Almera" (CSIC), Barcelona, Spain
[b] Department of Earth Sciences, Cornell University, Ithaca, NY, USA
[c] IFM-Geomar, Leibnitz Institut fuer Meereswissenchaften an der Universitaet Kiel, Kiel, Germany
[d] ICREA at Institute of Marine Sciences, CMIMA (CSIC), Barcelona, Spain

Received 19 April 2005; received in revised form 23 January 2006; accepted 30 January 2006
Available online 9 March 2006
Editor: V. Courtillot

Abstract

"Non-volcanic" rifted margins exhibit very little evidence of synrift magmatism, even where the continental crust has been thinned to such an extent that the mantle has been exhumed across a transitional zone (up to ~100 km wide), called the continent–ocean transition (COT). Using dynamical models of rifting, we explore how extension velocity, mantle composition and potential temperature influence the nature and extent of the COT and compare our results to observations at the West Iberia margin (WIM) and the ancient margins of the Liguria-Piemonte Ocean (LP) now exposed in the Alps. We find a first order relationship between extension velocity and the amagmatic exposure of mantle at the COT. For very slow half extension velocities, (<6 mm/yr), mantle exhumation begins before melting. At these velocities, by the time melting starts at the rift centre, the area of exhumed mantle has moved sideways creating a COT, the width of which increases with decreasing velocities. However, at 10 mm/yr, a velocity probably appropriate for the exhumation of mantle at the WIM and LP, melting starts prior to mantle exhumation. In this case, our models show that by the time mantle exhumation starts, a ~4.5 km column of melt has been produced, much more than the ~2 km maximum mean melt thickness inferred at the COT of these margins. Even considering that 25% of the produced melt may be trapped in the mantle, as in slow-spreading mid-ocean ridges, still more melt is produced in the models than inferred from observations. Thus, extension velocity alone cannot explain the practical absence of synrift magmatism at the COT of the WIM and LP. We find that the formation of a wide, amagmatic COT requires that either the mantle was depleted in basaltic constituents by >10% prior to rifting or that its potential temperature was ~50 °C lower than normal (≤1250 °C).

Keywords: non-volcanic margins; continent–ocean transition; melting; numerical modelling

1. Introduction

Continental rifting and the formation of new oceanic lithosphere involve a combination of magmatic and tectonic processes. At magma-poor, usually called "non-volcanic" rifted margins (NVRM), tectonic processes

* Corresponding author. Formerly at Department of Earth Sciences, University of Oxford, Oxford, UK and IFM-GEOMAR, Kiel, Germany.
E-mail address: mperez@ija.csic.es (M. Pérez-Gussinyé).
[1] Formerly at IFM-GEOMAR.

0012-821X/$ - see front matter © 2006 Elsevier B.V. All rights reserved.
doi:10.1016/j.epsl.2006.01.059

are responsible for thinning the continental crust and the subsequent exposure of the mantle along a wide zone, the continent–ocean transition (COT), which occurs before normal oceanic crust is generated. At the COT crustal separation is complete, only some allochtons of thin continental crust locally overlie the exhumed mantle (<3 km thick, e.g. Site 1069, Fig. 1), implying very large stretching factors in this area (>10). Similar whole lithosphere stretching factors would imply the generation of 6 km of melt at the COT (e.g. [1]). However, petrological and geophysical observations at these margins imply that magmatism was practically absent or scarce during mantle exhumation ([2–4]). It remains thus enigmatic to explain the conditions under which sub-continental mantle can be exposed along wide zones with little accompanying magmatism.

Non-volcanic margins include the West Iberia margin (WIM, [5,3,4]), the Newfoundland margin [6], most of the Labrador Sea conjugate margins [7,8], the south-east Australian margin [9] and the remnants of the margins of the ancient Liguria-Piemonte ocean (LP) of the Mesozoic Tethys now exposed in the Alps [10]. Of these, the best studied COT's come from the WIM, where three ocean drilling transects (ODP) and numerous geophysical surveys have been carried out, and from the Alps where parts of the remnants of the ancient margins of the LP margin can be observed directly.

At mid-ocean ridges the thickness of the basaltic crust is influenced by spreading velocity, temperature and composition of the upwelling mantle [11–13]. In this paper, we use finite element modelling (FEM) to explore the extent to which these factors inhibit melting during continental rifting and the transition to sea-floor spreading. We constrain the relative importance of these factors by comparing our results to the observations made at the COT's of the WIM and at the ancient margins of the LP ocean.

2. Constraints on rifting velocity at the WIM and LP margins

Both the Piemonte-Ligurian and Iberia-Newfoundland rifts experienced several extensional episodes from Late Triassic to Early Cretaceous [10]. Here we consider only the last rifting episode that was responsible for thinning the crust from 30 to 28 km to final break-up. The best constraints on rifting velocity come mainly from the Iberia Abyssal Plain segment (IAP) of the WIM (Fig. 1). During ODP Legs 149 and 173 pre-rift Tithonian sediments (~149 Ma, [14]) were recovered from the top of continental fault blocks at sites 901, 1065 and 1069 [15]. These sediments were deposited in a platform environment at few hundred meters depth, implying by isostasy that the crust was around 30–28 km thick at the time of deposition. Adittionally, at Sites 900 and 1067 (Fig. 1), where the crust is <6 km thick, lower crustal rocks were recovered with ^{40}Ar–^{39}Ar plagioclase ages indicating that they went through the 150 °C isotherm at 136–137 Ma [15,16]. Because these rocks are within the same footwall as mantle rocks that were exhumed 2 km oceanward (and recovered from ODP site 1068), it is inferred that they were very close to the base of the crust

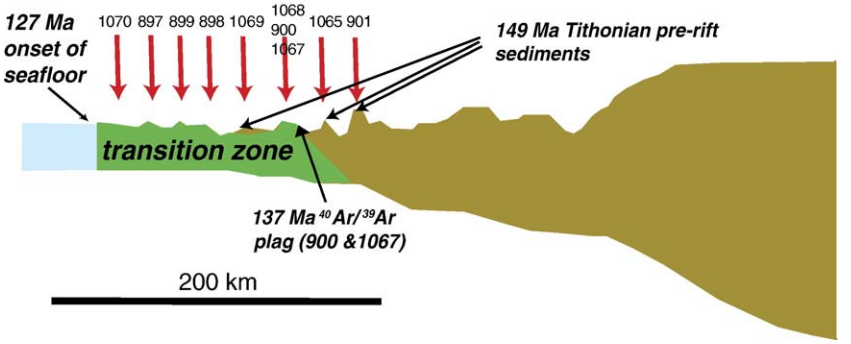

Fig. 1. Schematic cartoon showing the main constrains on the duration of rifting along the seismic line LG12 of the Iberia Abyssal Plain of the WIM. During ODP 149 and 173 pre-rift Thitonian sediments (149 Ma old, [14]) were recovered from the top of continental blocks at sites 901, 1065 and 1069 [15]. These sediments were deposited in a platform environment, implying by isostasy that the crust was ~28–30 km thick at the beginning of rifting, 149 Ma. At Sites 900 and 1067, where the crust is <6 km thick, lower crustal rocks were recovered with ^{40}Ar–^{39}Ar plagioclase ages indicating that they went through the 150 °C isotherm at 136–137 Ma [16]. Since these rocks are within the same footwall as mantle rocks that were exhumed 2 km oceanward (and recovered from ODP site 1068), it is inferred that they were very close to the base of the crust at the start of rifting at ~149 Ma [10,15]. This implies that the crust thinned form 28–30 km to <6 km in ~12–13 myr. The onset of seafloor spreading occurred around 127 Ma, thus more than 100 km of mantle were exposed during the period ranging from 136–137 to 127 Ma. This would correspond to a half rifting velocity of ~10 mm/yr for the phase of mantle exhumation.

at the start of rifting [10,15]. This implies that the crust thinned from 30–28 to <6 km in 12–13 myr (Fig. 1). Subsequently, exhumation of ~100 km of mantle occurred over 10–11 myr from 136/137 Ma until the onset of sea-floor spreading at 127 Ma ([17], Fig. 1). If the continental crust extended laterally by 50 km [18] between 149 and 137 Ma, we obtain a lower limit of 4.2 mm/yr half-rifting rate. We consider an upper limit to half-rifting rate of 10 mm/yr, this would correspond to exhume 100 km of mantle in 10 myr. This upper-limit is within the range at which sea floor spreading occurred westwards of the IAP (10–14 mm/yr half spreading rate, [17]) and is equal to that proposed for the ancient margins of the LP ocean [19].

3. Nature and extent of the COT at the WIM and LP margins

At the WIM, petrological and geophysical observations suggest that the COT consists of an expanse of exposed serpentinized mantle. The COT is 50–150 km wide and within the deeper part of the basement it contains discrete and elongated gabbroic intrusions increase in volume oceanward. This interpretation is suggested by wide angle data which show that the velocity structure of the COT is typical neither of thinned continental nor of magmatic oceanic crust [20], by multichannel seismic reflection data which show that the faulted blocks typical of thinned continental crust occur only locally at the COT [21,22], by the lack of strong magnetic anomalies characteristic of oceanic crust [23] and by serpentinised peridotite samples recovered from basement highs during ODP's 103, 149, 173 [2–4].

Geochemical analysis of cores drilled during ODP Leg 173 at the IAP and rocks exposed in the Alps suggest that the mantle exposed at the COT is subcontinental in origin [24,25]. The major and trace elements in the primary mantle minerals in samples from Alps and WIM, indicate that the subcontinental mantle was progressively modified by refertilization and melt-rock reaction during its exposure [25,26]. The spatial distribution of spinel and plagioclase peridotite in the COT of the Alps records the progressive process of melt extraction and thus the change from cold subcontinental mantle close to the thinned continental crust towards hotter 'oceanic-like' mantle further away from the thinned continental crust [25]. For example, in the Platta nappe in the Alps, melt extraction increases oceanward; gabbro bodies occupy less than 5% of the total serpentinized peridotite volume, but massive basalts, pillow breccias increase in abundance towards the ocean (e.g. [10] and references therein). These observations are in accord with results from modelling of magnetic anomalies along the COT of the IAP which indicate that close to the thinned continental crust the source bodies (probably intrusions) are discrete and deep within the basement (8 km into the basement), but oceanward become more closely spaced and shallower, eventually approaching the top basement [23].

To compare the modelling results with the observations we need to define a mean melt thickness that is representative for the amount of melt in the basement of the COT. However, because melt products come in the form of intrusions or pockets into the basement a mean thickness is difficult to define. We use Minshull et al. (2001) [18] estimates which suggest that the maximum mean melt thickness that is compatible with the wide-angle seismic velocities and the inversion of magnetic data is 2 km. This would be equivalent to assume that the upper seismic velocity layer in the COT contains only 10% of frozen melt, which is compatible with the observation that magnetic bodies tend to be at deep in the basement [23], and that the lower velocity layer, where velocities are around 7.5 km/s, consists of c. 40% of frozen melt products. In the next sections we will use this maximum mean estimate of melt emplacement to discriminate to what extent rifting velocity, mantle potential temperature and composition can account for the formation of a wide COT at non-volcanic margins.

4. Numerical model

Our dynamical model is built to simulate the key rheological and chemical changes which occur during extension at NVRMs. These include: 1) progressive embrittlement of the lower crust during extension [27], 2) mantle serpentinisation once the crust becomes brittle and faults allow abundant water to reach the mantle [27–29] and 3) the accompanying decompression melting as the lithosphere thins.

We use a 2D finite element (FEM) Newtonian viscous flow solver based on a penalty function method [30], coupled with a finite difference technique for the advection and diffusion of heat [31]. Our code was originally developed for studying mid-ocean ridge dynamics [32]. We have incorporated 1) an iterative scheme over the Newtonian viscosity so that the maximum differential stress does not exceed the yield strength envelope determined from the brittle and ductile (non-Newtonian) rheologies [33] in both crust and mantle (see Appendix and Fig. 2 for rheological parameters used), 2) melt production taking into account

the effect of increasing depletion in the solidus temperature (following [34]), 3) serpentinite production (see Appendix), 4) the increase of temperature due to the exothermic nature of serpentinisation, (see Appendix) 5) the decrease in the friction coefficient where serpentinisation occurs (see Appendix), 6) increase of the thermal conductivity throughout the brittle crust due to hydrothermal circulation (following the treatment in [35]). Additionally, we have incorporated tracer particles that allow us to track the Moho and determine when the entire crust becomes brittle (using the tracking method in [36]). At this point, if the mantle is within the temperature stability field for serpentinite, serpentinisation is set to start. We also use tracer particles to track the position of the serpentinised mantle and the base of the continental lithospheric mantle during the model runs. Details on the rheology, calculation of the temperature field and the melt and serpentinite production can be found in the Appendix.

4.1. Initial conditions

Crustal and lithospheric thickness are meant to simulate the starting conditions at NVRMS (see caption of Fig. 2). The initial temperature at the Moho is 550 °C and that of the lithosphere's base is between 1200 and 1300 °C, depending on the numerical experiment. The temperature at the Moho is meant to reflect the 500–600 °C Moho temperature range obtained from analysis of pressure–temperature–time (P–T–t) paths of rocks recovered from the Alps and WIM [37,38]. Furthermore, reconstruction of the initial geotherm at various NVRMs indicates that these rather cold initial conditions might have been common at many non-volcanic margins [39].

The finite element mesh used was initially symmetric, with a thicker crust at the rift centre than at the rift sides so that extension localizes at the mesh centre (see Fig. 2). Seismic data from the West Iberia-Newfoundland conjugate margins shows that there is an asymmetry in the pattern of thinning of continental crust prior to break-up [40]. However, results of ODP 210 in the Newfoundland margin have been interpreted to show that none of the COT's of the WIM-Newfoundland conjugate margins were formed by normal seafloor spreading but by amagmatic exhumation of mantle on both sides of the rift [41]. Therefore, we choose to use an initial symmetric mesh and let the system evolve according to its changing rheology and temperature field.

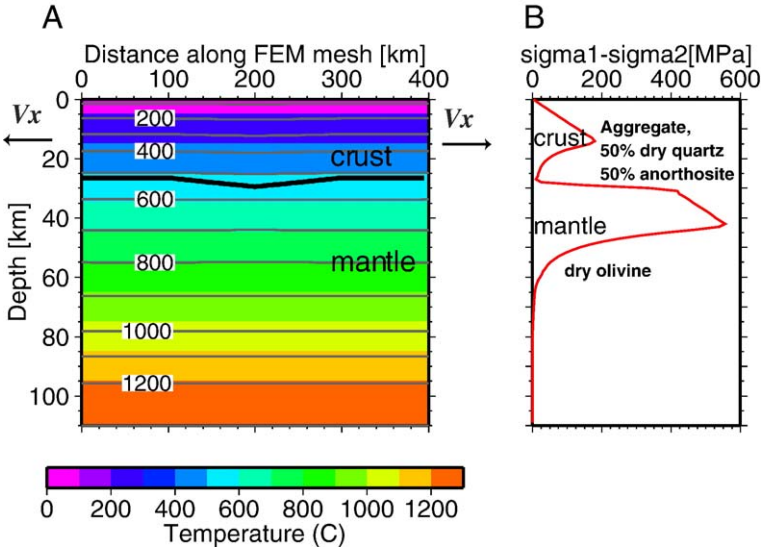

Fig. 2. (A) Schematic cartoon showing the geometry of the finite element mesh and the initial temperature. The crust is 29 km thick at the centre of the mesh, so as to simulate the platform conditions existing at the start of rifting. To localise the deformation during the model run we let the crust thin to 26 km at both ends of the FEM mesh. The base of the lithosphere is at 110 km and reflects the lithospheric thickness onshore West Iberia [65]. The initial temperature at the Moho is of 550 °C, within the 500–600 °C temperature range suggested from P–T–t paths in the Alps [37] and in the WIM [38]. The temperature at the base of the lithosphere is between 1300 and 1200 °C, as indicated in the Results section. Heat flux and radiogenic heat production are adjusted as to match the Moho and base of the lithosphere's temperature. Vx is the velocity applied on each side of the model. (B) Initial rheological profile from a visco-plastic rheology. In the crust the differential stress is bounded by Byerlee's law and by the power law for an aggregate consisting of 50% dry quartz and 50% anorthosite [53]. In the lithospheric mantle the maximum differential stress in the ductile regime is given by the dry olivine power law [54].

4.2. Boundary conditions

The deformation of the model is driven by a constant velocity boundary condition applied to its sides. We have made this boundary condition choice because it is computationally simple. However, at the WIM there is evidence that the velocity increases with time ([15,10]). In our models, although the velocity is constant on either side of the FEM mesh, the strain rate changes as a function of the evolving viscosity. Weakening of the rift centre related to the increased geothermal gradient leads to a viscosity reduction, localisation of extension and thus an increase of the strain rate in this area. In order to simulate the rift acceleration observed at the WIM either more stress-dependent rheologies or a constant stress boundary condition should have been used, both of which are more complicated to implement. We 'by-pass' this problem by comparing the observations of crustal thinning to those obtained with a constant velocity boundary condition of 6 mm/yr and the observations of

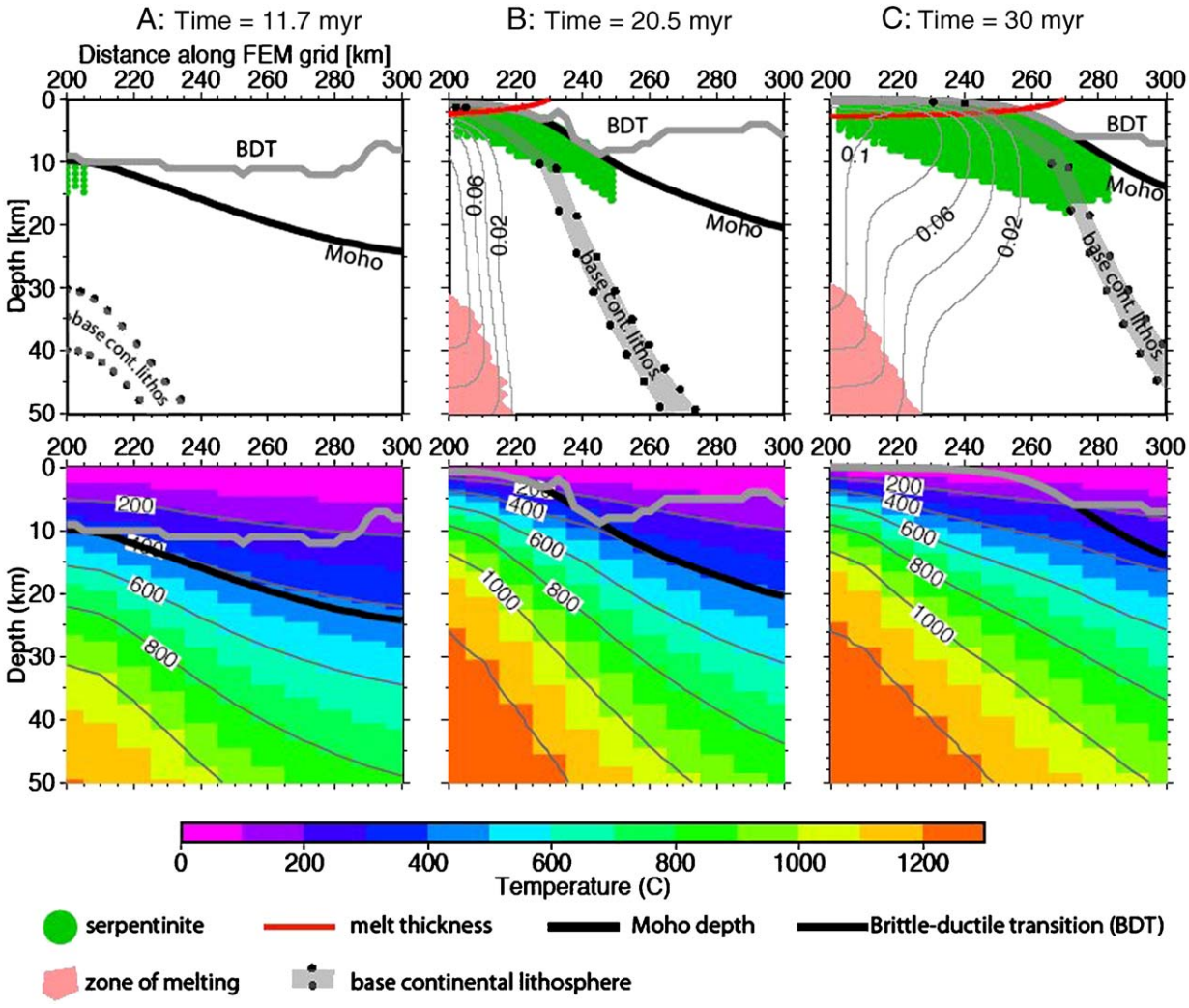

Fig. 3. Model evolution for a velocity of 4.2 mm/yr applied to each side of the FEM mesh and a mantle potential temperature of 1300 °C. Three snapshots in time are shown corresponding to (A) the time at which the entire crust becomes brittle, (B) the time at which the mantle is first exposed at the surface and (C) time at which the melt production has become steady-state. On the top panels the position of the brittle–ductile transition (BDT), Moho, the serpentinised mantle, and the base of the continental lithosphere are shown for each time step. The Moho, serpentinised mantle and base of the lithosphere are followed through time with tracer particles. The area where melt is produced during that time of the model run is shaded in pink. The grey contours show the amount of depletion of the residual mantle after melting during rifting. The contours are every 0.01, which corresponds to 1% of depletion. The red line shows the total thickness of melt that would be in the basement if all the melt would be focused at the rift centre and moved sideways with a velocity equal to that prescribed at the sides of the FEM mesh. On the bottom panels are the temperature field corresponding to each time step, overlain by the position of the Moho and the brittle–ductile transition.

mantle exhumation with the results obtained with a velocity of 10 mm/yr (see Discussion section).

4.3. Melt migration

In this paper, we consider that the melt produced at depth over a wide area migrates towards the surface into the zone of maximum strain rate. We base this assumption on the observation that even at ultra-slow spreading ridges (where half spreading rates are ≤ 10 mm/yr), such as the Gakkel ridge, the area of new ocean crust production is restricted to a narrow median volcanic ridge [13]. In all of our experiments by the time melt production starts, the strain rate is already strongly localized at the centre of the FEM mesh. Thus, to calculate the melt thickness along the COT, we migrate the melt produced during a given time interval towards the centre. In the next time step, we move the melt laterally away from the centre with a velocity equal to the rifting velocity applied on each side of the FEM mesh. The melt thickness obtained along the COT should be regarded as an upper bound estimate as some melt might be trapped in the mantle during its ascent, as it is inferred for the COT of the LP and at slow spreading ridges [42,43].

5. Results

Our results (Figs. 3–7) show how the lithosphere evolves with time during extension and illustrate the effects of changing extension velocity, mantle potential

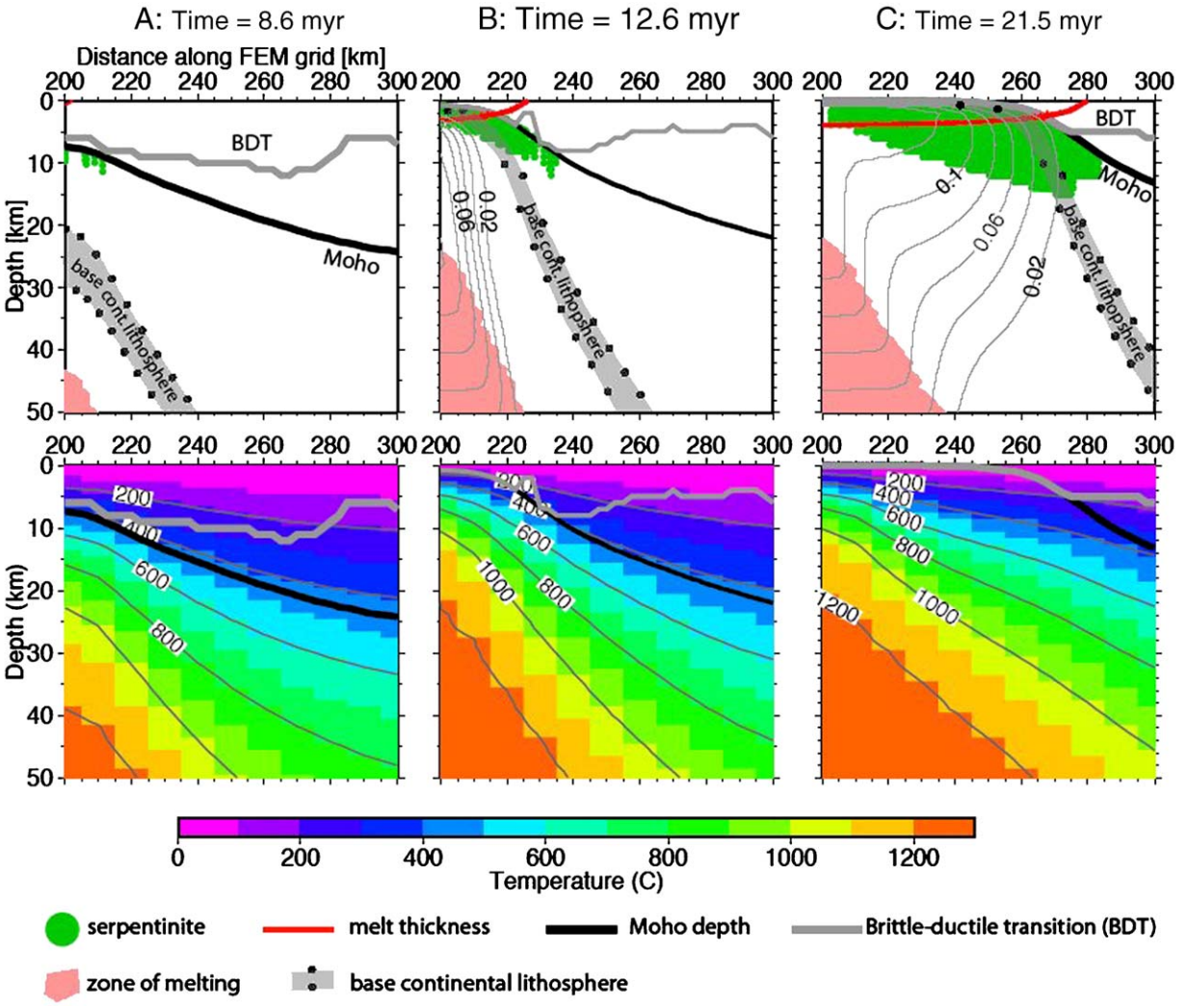

Fig. 4. The same as in Fig. 3 but with a velocity of 6 mm/yr applied to side each of the FEM mesh and a mantle potential temperature of 1300 °C. Note that at this velocity serpentinisation and melt production start simultaneously.

temperature and composition. Only the right hand side of the model is shown. The figures show from left to right three snap shots in time during rifting. In all the models, the rocks cool and decompress during extension so that after a certain time, the entire crust at the centre of the rift becomes brittle. Crustal embrittlement is followed by serpentinisation of the underlying mantle, crustal separation and exposure of the mantle at the COT. We also show the degree of depletion of the exposed mantle as a consequence of melting during rifting. Our results, show that the degree of depletion increases towards the ocean. This is in agreement with the chemistry of mafic liquids which record an increase in melting oceanward and a decrease in contamination by an enriched, possibly subcontinental, component in the same direction [44].

In order to compare the final amount of melt in the COT produced by each of the models, we show in Fig. 8 a plot of the melt thickness (assuming all melt is focused at the rift centre) as a function of distance from the 10 km thick crust. In this section we describe the effects of varying the extension velocity, mantle potential temperature and composition on the nature and extent of the COT.

5.1. Effect of extension velocity

Figs. 3–5 show how the lithosphere evolves in time when three different extension velocities are applied to

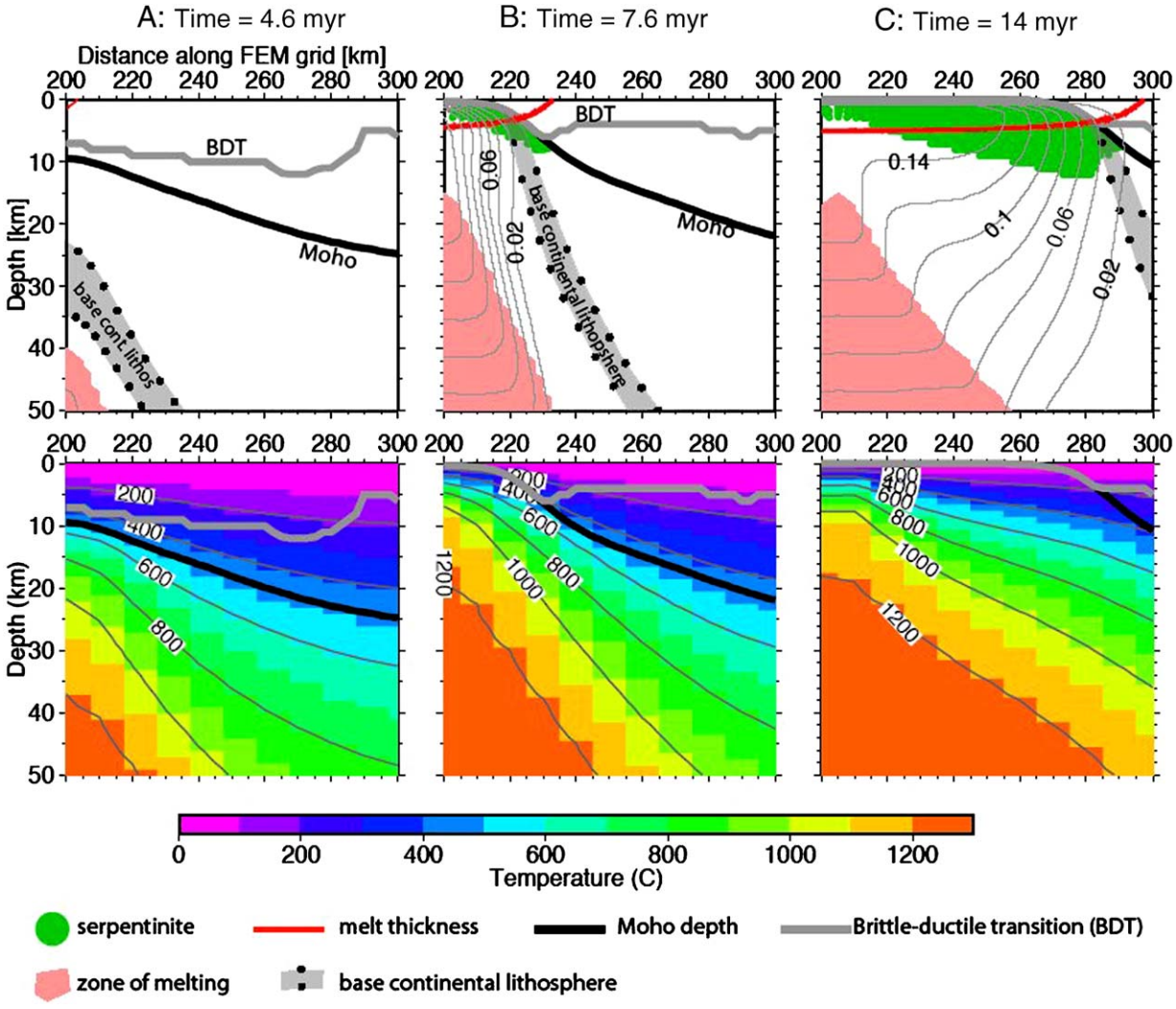

Fig. 5. The same as in Fig. 3 but with a velocity applied to the mesh sides of 10 mm/yr and a mantle potential temperature of 1300 °C. Note that at this velocity melt production starts before serpentinisation, and thus in (A) the time at which melting starts is shown. (B) and (C) correspond to the same moments during the model run as in Fig. 3.

its sides, 4.2, 6, and 10 mm/yr. The figures show that when the extension velocity is high, melt production starts before serpentinite production (Fig. 5A). On the other hand, when the extension velocity is slower (Figs. 3A and 4A) serpentinite production starts before or simultaneously with melt production. At this stage, serpentinite is formed near the surface, while magma generation either has not started (Fig. 3A) or it is still at >40 km depth (Fig. 4A). With increasing time and extension, the serpentinised region is moved laterally and the melting region migrates upwards but remains focussed at the centre of the rift (Figs. 3B and 4B). Although melting occurs during the phase of mantle exhumation, if the melt is focused at discrete eruption sites and part of it is trapped in the mantle, it would be possible to expose a wide region of exhumed mantle with a small volume of syn-rift melt products before the steady-state thermal and magmatic structure of a ridge has been developed.

In addition, Figs. 3–5 illustrate how the zone of exhumed mantle narrows with increasing extension velocity. For example, for the highest velocity used here, melting starts prior to crustal embrittlement (Fig. 5A). This implies that when crustal separation occurs (Fig. 5B), the amount of melt that has already been produced is considerable and the zone where melting occurs extends up to near the surface, suggesting that most of the melt produced will be erupted to the surface before a significant width of mantle rocks may be exposed. As a result, it is likely that at faster rifting

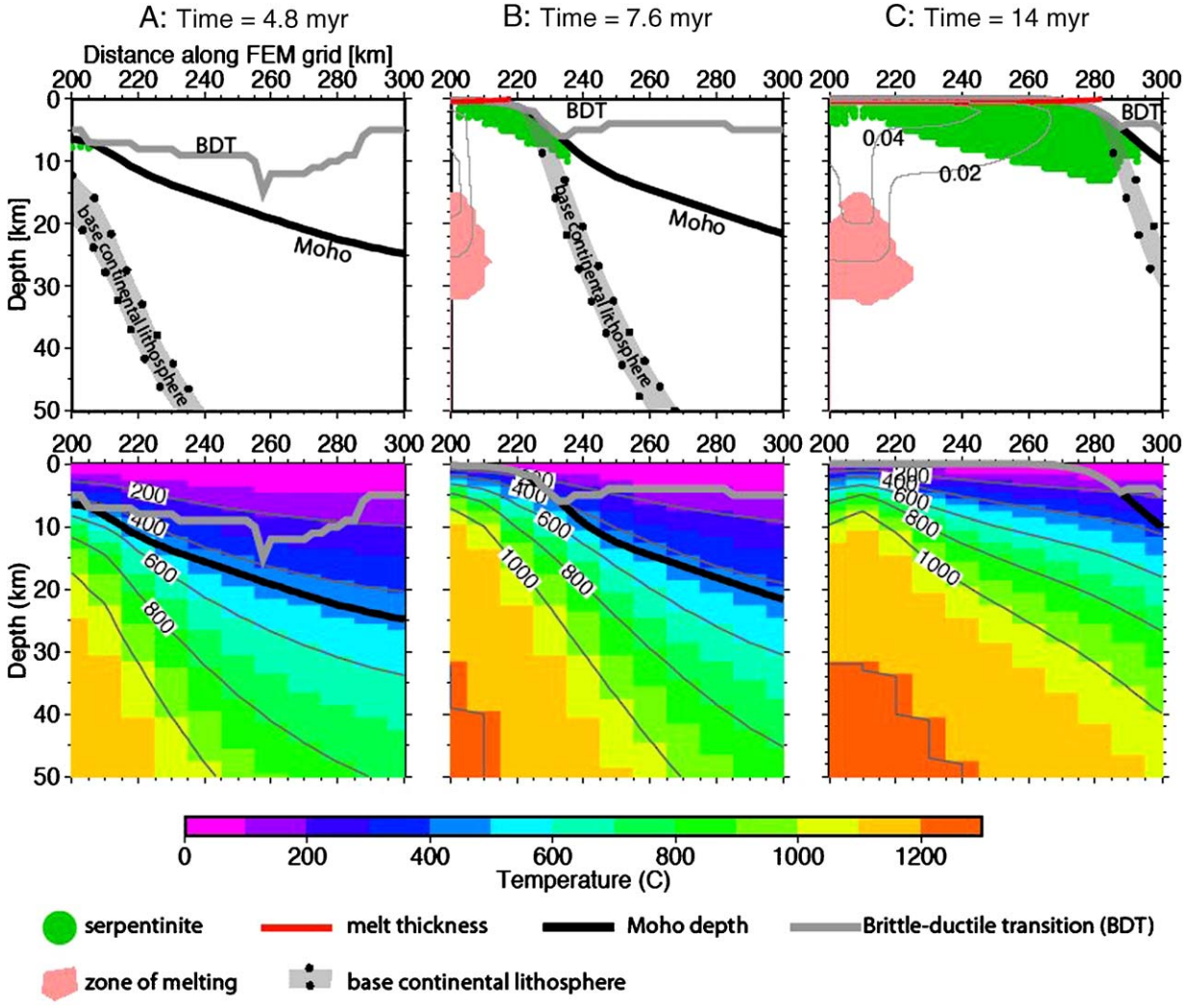

Fig. 6. Illustration of the effect of the mantle potential temperature on melting at the COT. The mantle potential temperature is 1200 °C and v = 10 mm/yr. (A), (B) and (C) represent the same moments during the model run as in Fig. 3. Note how the amount of melt is reduced along the COT in comparison to Fig. 5.

velocities the transition from rifting to seafloor spreading is marked by a sharper transition in both space and time.

5.2. Effect of mantle temperature

In Fig. 6, the effect of a cooler sub-lithospheric mantle is explored. For the fastest extension velocity studied here (10 mm/yr) and a mantle potential temperature of 1200 °C a very small amount of melt (<1 km, Fig. 8) is generated even long after complete crustal separation has occurred. Therefore, a wide area of serpentinised mantle is exposed at the surface. At the same velocity, when the potential temperature is 1250 °C, the amount of melt produced is similar to that produced with a potential temperature of 1300 °C and a very slow velocity, 4.2 mm/yr (Fig. 8). Cool sub-lithospheric mantle is thus an effective way of explaining the exhumation of wide regions of mantle with little or no products of syn-rift melting, as observed off west Iberia.

5.3. Effect of mantle composition

Several authors have suggested that the extent of melting at mid-ocean ridges might be influenced by the chemical composition of the mantle [13]. In particular, because the peridotite solidus temperature increases after melt extraction, a more depleted composition of the mantle would lead to less melting. We have explored

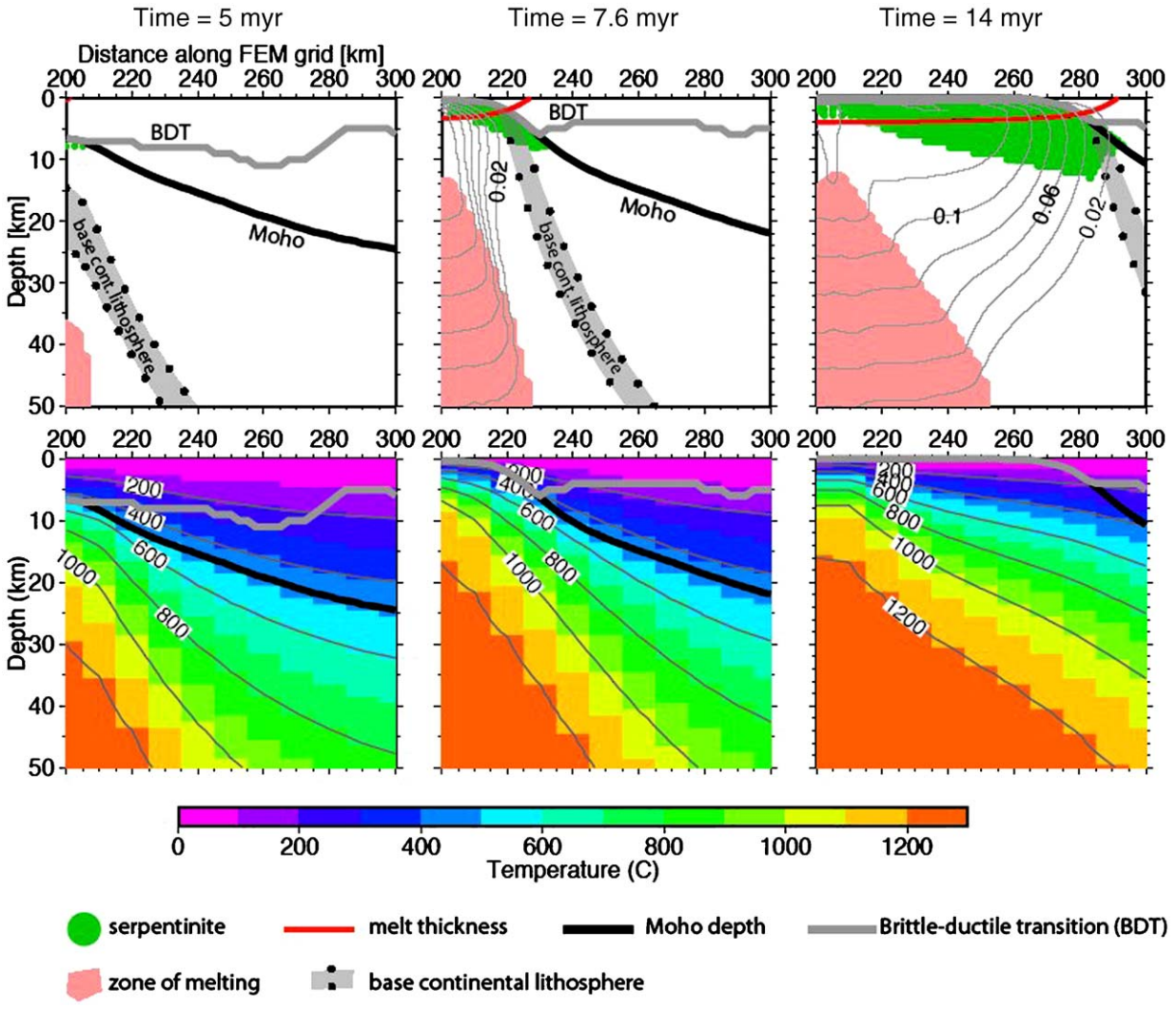

Fig. 7. Illustration of the effect of the mantle composition on melting at the COT. The velocity boundary condition is 10 mm/yr, mantle potential temperature is 1300 °C and the mantle is depleted by 10% at depth levels where the temperature <1300 °C. (A), (B) and (C) represent the same moments during the model run as in Fig. 3. Note that the amount of melt produced is reduced in comparison to Fig. 5.

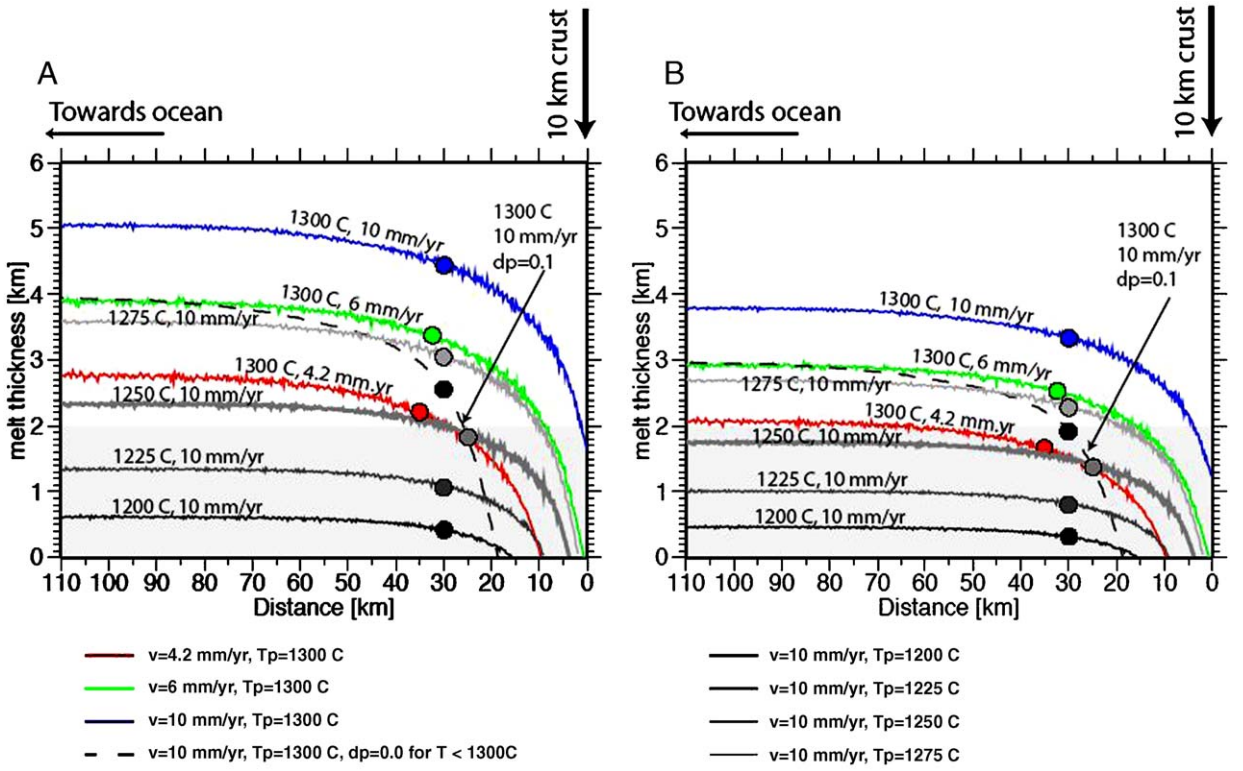

Fig. 8. Melt thickness that would be expected at the COT as a function of the distance from the 10 km thick continental crust. Each curve represents the result for model runs with different velocities and/or mantle temperature or composition (see legend). The grey shaded area represents the potential maximum mean melt thickness that could be in the COT of the WIM [18]. Circles mark the location where the crust is computed to be thinner than 1 km. We consider this position to correspond to the location where mantle is exhumed at the surface. In (A) all melt is assumed to migrate at the rift centre and move sideways with a velocity equal to that applied to the sides of the FEM mesh. Note that 10 mm/yr is an appropriate velocity for the exhumation of mantle in the COT (see Constraints on rifting velocity at the WIM and LP margins section). In this case, for a normal mantle potential temperature, T_p=1300 °C, ~4.5 km of melt have been produced at the location where the mantle is first exhumed at the surface (marked by the blue circle). This is much larger than the mean maximum melt thickness of 2 km. In (B) the same results as in (A) are shown but here 25% of the melt produced is assumed to stagnate in the mantle [43]. Note that for the case of 10 mm/yr and T_p=1300 °C, the melt thickness produced at the time of mantle exhumation is still larger than the maximum potential mean melt thickness in the COT. Hence if melt stagnation in the mantle is no more than 25%, other factors such as mantle temperature or composition must be key in explaining the scarce melt at the COT of non-volcanic margins.

the effect of a refractory mantle composition by assuming that all the material which is at a temperature <1300 °C is depleted by 10% prior to melting during rifting. This situation is simulated by forcing the solidus within the depth levels where the temperature is <1300 °C, to correspond to the solidus resulting from 10% depletion. In this case (Figs. 7 and 8), the onset of melting is delayed in comparison to the case where the mantle is fertile (Figs. 5 and 8). This is because the depth levels which first melt, i.e. between 1200 °C and 1300 °C have a higher solidus. Also, when melting starts, the amount of melt produced is reduced by about 1 km with respect to the case where the mantle is fertile along the COT (Fig. 8).

6. Discussion

We have explored the effect that decreasing velocity, mantle temperature and composition have on the nature and extent of the COT. For the phase of crustal thinning the half extension velocity of 6 mm/yr appears to best fit the observations. For example, at this velocity the mantle is exhumed for the first time at the surface after 12.6 myr (Fig. 4), similar to the time that elapsed to thin the continental crust from around 28–30 km (at 149 Ma) to <6 km (at 137–136 Ma) at the IAP (Fig. 1). The phase of mantle exhumation is better described by the 10 mm/yr velocity (Fig. 5). In this case, the system takes ~10 my to evolve from a situation where the crust is 10 km thick at the rift centre (Fig. 5A) to a

situation where ~70 km of mantle have been exposed at the surface (see section Constraints on rifting velocity at the WIM and LP margins). Hence, we assume that melt production in the COT of the WIM must have been similar to that produced with the 10 mm/yr case shown here. At this velocity, assuming a mantle potential temperature, T_p, of 1300 °C, by the time the mantle is exhumed at the surface, 4.5 km of melt have been already produced (Fig. 8). Moreover, the mean melt thickness at the COT is 5 km (Fig. 8). This is much larger than the 2 km maximum melt thickness predicted in the COT of the WIM from wide-angle data and inversion of magnetic anomalies ([17,18], Fig. 8A).

During melt migration it is possible that some of the liquid crystallizes on a conductive geotherm in the mantle, so that the melt produced might not all reach crustal levels [45]. Based on field, petrological and geochemical studies of the peridotites of the COT exposed in the Alps, Piccardo et al. (2004) [42] suggested that this is actually the case: "the presence of large areas of impregnated peridotites indicates that significant volumes of melts were trapped in the lithospheric mantle". Unfortunately, to our knowledge, there are no estimations in the literature of the amount of melt trapped in the mantle during continental extension and the formation of the COT. As slow or ultra-slow spreading oceanic ridges are the best analogue to the tectonic process leading to the formation of the COT, we use estimations of the melt trapped in the former as a guide for the potential amount of melt trapped in the latter. At slow-spreading mid-ocean ridges, Cannat [43] suggested that at the maximum amount of melt trapped in the mantle might be 25%. If we subtract this 25% from the total melt produced during the formation of the COT, with a 10 mm/yr velocity and T_p=1300 °C, the resulting melt thickness along the COT is ~3.8 km (Fig. 8B). This thickness is still larger than the potential maximum of 2 km (Fig. 8, [18]). Thus, if 25% is a correct upper-bound for melt stagnation in the mantle, our modelling supports that the lack of magmatism at the COT cannot only be a function of extension velocities; potential mantle temperature or composition might be key in explaining the small amount of magmatism observed. This situation resembles that of the ultra-slow spreading Gakkel ridge, where the amount of magmatism does not have a linear relationship to spreading velocity [13].

Mantle composition can considerably reduce melt production provided the degree of depletion at the lithosphere's base is sufficiently large prior to rifting (>10%, Fig. 8). Our models predict that when the base of the lithosphere is depleted by 10%, the melt thickness along the COT is ~4 km (vel. of 10 mm/yr, Fig. 8A). After subtracting a 25% of melt which might stagnate in the mantle, the predicted melt is still 1 km thicker than the potential maximum of 2 km (Fig. 8B). Therefore, in order for mantle composition to be the only factor responsible for the scarce magmatism at the COT, the basal lithospheric depletion needs to be >10% prior to rifting. In the LP, Muentener et al. (2004) [25] have found that the exhumed mantle was depleted prior to Jurassic rifting. Also, the WIM peridotites appear to belong to the Ronda, Beni Boussera depleted end-member [23]. However, in the WIM as well as the LP, the exact degree of depletion is not known. For the Ronda peridotite the depletion is high, 15–30%, but these estimates focus on rocks thought to have melted to this degree at much shallower depths [46,47]. Hence, it is unclear that this degree of depletion can be assumed for the continental lithosphere's base.

An alternative way of exposing the mantle at the COT with little accompanying magmatism is to consider that it was cooler than that which produces normal thickness oceanic crust [48]. Our results show that only a reduction of 50 °C of the mantle potential temperature is required to decrease the amount of melt along the COT to ~2 km thickness (Fig. 8A,B). Spatial variations of mantle potential temperature, T_p, have been deduced elsewhere, for example from the anomalously large mid-ocean ridge depths in the equatorial Pacific and Indian oceans [49] and in particular from petrological data for the central Atlantic [50]. This T_p anomaly has led to the exposure of a >500 km long continuous strip of oceanic lithosphere free of basaltic crust, with scattered blobs of frozen melt [51], reminiscent of the COT off the WIM and LP. If the subcontinental mantle is, in general, cooler than the oceanic one [48], ultimately, the production of normal thickness oceanic crust would be related to the availability of fertile, hot, plume-fed oceanic asthenosphere, as suggested by [52].

7. Conclusions

We have used a dynamical model to explore the mechanisms by which a wide zone of sub-continental mantle with little accompanying magmatism can be exposed prior to the onset of sea-floor spreading at non-volcanic margins. We have shown that at rifting velocities adequate for extension at non-volcanic margins, very little melt is produced before the crust has thinned

to around 10 km. Ongoing extension leads to crustal separation and exhumation of the mantle. Serpentinisation starts once the entire crust is brittle and continues as the mantle is exposed at the COT. The extension velocity controls whether mantle exhumation occurs prior to the onset of melting and also the width of the areas of transitional nature between continental and oceanic crust. For half-rifting velocities <6 km/myr mantle exhumation and its serpentinisation occur prior to melting. Serpentinites are generated at the surface or at very shallow depths whereas the melt is generated much deeper. As a result, if part of the melt is trapped in the mantle during its ascent, a broad area of serpentinised and exhumed sub-continental mantle can be exposed with isolated magmatic intrusions which increase in volume oceanward. However, for the extension velocities adequate for the WIM and LP, 10 km/myr, ~3 km of melt should be trapped in the mantle to reproduce the maximum potential thickness of melt predicted by wide-angle and magnetic data at the COT. Thus, we suggest that other factors contributed to the reduced melt production during exposure of the COT at non-volcanic margins.

A refractory mantle composition can lead to a reduction of melt production. However, the mantle depletion prior to melting during rifting should be larger than 10%, as our results indicate that a 10% depleted mantle would produce, at least, 1 km more of melt than the maximum mean melt thickness inferred along the COT of the WIM.

An alternative way to generate a wide zone of exposed mantle with little magmatic products is to consider that the mantle potential temperature, T_p, at non-volcanic margins is lower than 1300 °C. Our results show that a T_p reduction of only 50 °C would be required to lower the melt thickness to the 2 km inferred from wide angle data along the COT of the WIM. If the mantle was indeed ≤1250 °C, normal oceanic thickness could only be generated when hotter plume-fed material propagated into the continental rift.

Acknowledgments

We thank L. Geoffroy and two anonymous reviewers for their comments which helped to improve the paper. We also thank L. Ruepke for providing the routines to model tracer particles and for discussions on the methods. This work was done under a DFG grant to T. Reston, a NERC (National Environmental Research council, UK) and a Ramón y Cajal fellowship (from the Education and Science Ministry of Spain) to M. Perez-Gussinyé.

Appendix A. Flow field

The flow field is calculated by solving for the conservation of momentum (1) and mass (2) of an incompressible Newtonian fluid:

$$\tau_{ij,j} - p,_i - \rho g_i = 0 \quad (1)$$

$$u_{i,i} = 0 \quad (2)$$

$$\tau_{ij} = 2\eta \dot{\varepsilon}_{ij} \quad (3)$$

where τ_{ij} is the deviatoric stress tensor, u_i is the velocity in the ith direction, p is pressure, ρ the density, g the gravity and η the viscosity. The first equation describes the force balance after neglecting the inertial terms (i.e. assuming Stokes flow). In practice, because the viscosity is large within the lithosphere we neglect the buoyancy force (i.e. $\rho g_i = 0$). The second equation expresses the conservation of mass for an incompressible fluid and the third is the constitutive equation for a Newtonian fluid in terms of the deviatoric stress.

The boundary conditions consist of prescribing constant horizontal velocity at each side of the grid and vertical velocity equal to zero at the top of the grid.

Appendix B. Rheology

The rheology is that of a multilayered visco-plastic material. The viscosity corresponds to that of a Newtonian fluid which cannot exceed a given yield stress. The yield is defined at each point in the mesh by Byerlee's law or a power law rheology (consisting of an aggregate of 50% anorthosite and 50% dry quartz in the crust [53], and dry olivine in the mantle [54]). At each time step, if necessary, the viscosity is reduced iteratively in order that the differential stress does not exceed the plastic yield. The iteration scheme are as follows.

B.1. Brittle field

In the brittle field the maximum differential stress is given by Byerlee's law [55] which in terms of principal stresses and the depth, z, is:

$$(\sigma_1 - \sigma_3)_{brit} = 1 + 12.7z$$

On the other hand, the differential stress of a Newtonian fluid with a viscosity η_{old} is related to the fluid velocities by:

$$(\sigma_1 - \sigma_3)_{old} = 2\eta_{old}((u_{i,j} + u_{j,i})^2 + 0.25(u_{i,j} - u_{j,i})^2)^{1/2}$$

The new 'effective brittle' viscosity, η_{newb}, is found by equating the differential stress for a Newtonian fluid to the brittle yield stress:

$$(\sigma_1-\sigma_3)_{new} = 2\eta_{newb}((u_{i,j}+u_{j,i})^2+0.25(u_{i,j}-u_{j,i})^2)^{1/2} = (\sigma_1-\sigma_3)_{brit}$$

hence,

$$\eta_{newb} = ((\sigma_1-\sigma_3)_{brit}\eta_{old})/(\sigma_1-\sigma_3)_{old}$$

The new viscosity, η_{newb}, is input in the flow program where the velocity field is solved again assuming that the fluid is Newtonian. Subsequently η_{newb} becomes η_{old} and the iteration is repeated until the difference between the old differential stress and the new is negligibly small.

B.2. Ductile field

At high temperatures yielding of rocks has been shown to occur by creep flow. Creep can occur by Newtonian diffusion creep and non-Newtonian dislocation creep. In the Earth, diffusion and dislocation creep may occur simultaneously within a crystal. Gueguen and Darot (1982), [56], observed samples of olivine with transmission electron microscopy and found evidence for both dislocation and diffusion creep which led the authors to propose the mechanisms act as concurrent parallel processes.

A general constitutive law for polycrystalline flow is given by Karato and Wu (1993) [57]:

$$\dot{\varepsilon} = A(\sigma/\mu)^n(\boldsymbol{b}/d)^m\exp(-(E+\mathrm{PV})/\mathrm{RT})$$

where μ is the shear modulus (80 GPa), n the stress exponent, $\boldsymbol{b}$ the length of the Burgers vector, d the grain size, m the grain-size exponent, E the activation energy, V the activation volume, P the lithostatic pressure, R the gas constant, and T the absolute temperature. The term PV is only important under deep asthenospheric conditions, so for simplicity we do not use it.

In order to find the ductile effective viscosity, η_{newd}, we need to formulate the flow law in terms of the stresses, σ_{ij}, and strain rates, $\dot{\varepsilon}_{ij}$, in the FEM coordinate system. In terms of the deviatoric stress tensor, σ'_{ij}, and invariants of the stress, $\sigma_e=(\sigma'_{ij}\sigma'_{ij})^{1/2}$, and strain rate tensor, $\dot{\varepsilon}_e=(0.5(\dot{\varepsilon}_{ii}^2+\dot{\varepsilon}_{jj}^2)+\dot{\varepsilon}_{ij}^2)^{1/2}$ the flow law is:

$$\dot{\varepsilon}_{ij} = A(\sigma_e')^{1-n}\sigma_{ij}(1/\mu)^n(\boldsymbol{b}/d)^m\exp(-E/nRT)$$

$$\sigma_e^n = A\dot{\varepsilon}_e$$

Finally, the new effective ductile viscosity, η_{newd}, relates the stress and strain rate:

$$\sigma_{ij} = \eta_{newd}\dot{\varepsilon}_{ij}$$

and hence is equal to:

$$\eta_{newd} = \varepsilon_e^{(1/n-1)}A^{-1/n}\mu^n(d/\boldsymbol{b})^m\exp(E/nRT)$$

The expression for viscosity adopted allows for either diffusion creep or dislocation creep, depending on the values used for the parameters. Diffusion creep is Newtonian ($n=1$), in this case, the strain rate factor drops out of the viscosity expression. Dislocation creep is non-Newtonian ($n>1$), and so the strain rate factor remains, but the grain size exponent $m=0$.

We consider that either dislocation or diffusion creep can dominate depending on the physical conditions. If these two mechanisms are independent or simultaneously occur, then they can be considered to act as dashpots in series. In this case, the strain rate is the sum of the two independent strain rates and the mechanism that dominates is the one that yields a higher strain rate.

$$\dot{\varepsilon}_{total} = \dot{\varepsilon}_{diffusion} + \dot{\varepsilon}_{dislocation}$$

$$\dot{\varepsilon}_{diffusion} = \sigma/\eta_{diffusion}$$

$$\dot{\varepsilon}_{dislocation} = \sigma/\eta_{dislocation}$$

The net or effective viscosity is then given by summing the contributions from each rheology.

$$\eta_{total} = (1/\eta_{diffusion} + 1/\eta_{dislocation})^{-1}$$

In practice, because of problems of instability, we added a minimum constraint to viscosity. We imposed the viscosity to be higher than a small fraction of the viscosity at the base of the lithosphere. This was done by adding a third dashpot in series with viscosity $\eta=\eta_{min}/7000$, where η_{min} is the viscosity at the base of the FEM grid.

To calculate the final viscosity at each depth, the effective strain rate is first calculated assuming a Newtonian viscosity. If the differential stress is greater than the ductile differential stress then a new viscosity is found with which the flow is calculated again. This process is iterated several times until the difference between the old and new differential stress is small.

Appendix C. Temperature calculation

The temperature equation is calculated with a finite difference scheme that takes into account the conduction and advection of heat in the vertical and horizontal

coordinates, the heat of fusion consumed by decompression melting whenever this occurs, the heat generated by the serpentinisation reaction whenever it occurs and the decrease in thermal conductivity produced by hydrothermal circulation at the shallow depths.

The temperature equation can be written as:

$$T^{c}_{,t} = \kappa(T^{c}_{,ii} + T^{c}_{,jj}) + u_i T^{c}_{,i} + u_j T^{c}_{,j} - L' F_{m,t} + H_s F_{s,t} + H(z)/\rho C_p$$

where T^c is the temperature corrected for adiabatic effects: $T^c = T_{true} - \gamma z$, where T_{true} is the real temperature and γ is the adiabatic gradient, t is time, u_i and u_j are horizontal and vertical velocities, $F_{m,t}$ is the melt production rate (units in fraction/time) and L' is the latent heat of melting (or heat of fusion), which we convert here into an effective 'superheat' of 600 °K [58]. H_s is the heat released when water reacts with olivine to produce serpentinite which has been converted to an effective heat of serpentinisation of 300 °K, from the enthalpy of the peridotite–serpentine reaction (e.g. [59]). $F_{s,t}$ is the serpentinite production rate. $H(z)$ expresses the distribution of radioactive heat in the crust and ρ and C_p are the crustal density and the heat capacity.

Hydrothermal circulation is assumed to occur throughout the duration of extension at crustal depths where brittle fractures exist and where the temperature is lower than 600 °C. The effect of hydrothermal circulation is modelled as an increase of the thermal conductivity by a factor β wherever it occurs [35].

The calculation of the melt production is explained in detail in [34,39]. In the next section the procedure to find the serpentinite production is explained.

C.1. Serpentinisation

At the WIM serpentinisation of the sub-continental mantle started beneath the edge of the thinned continental crust (see [10] and references therein). A major condition for serpentinisation to occur must have been that the entire crust was in the brittle regime so that large amounts of fluids could reach the mantle (see review in [27]) and that cracks that functioned as fluid conduits were kept open (i.e., the faults were active and permeable). Serpentinisation also requires peridotite at appropriate temperature conditions. The maximum temperature at which serpentine can develop varies somewhat depending on the serpentine mineral under discussion and the study carried out. In this study we used an upper limit for serpentinisation of 500 °C [60,61]. Thus, we allow serpentinisation to occur only at the locations where the entire crust is brittle and the temperature in the mantle is below 500 °C. These locations are allowed to move with the flow field and are shown by the green dots in Figs. 3–7.

C.2. Effect of serpentinite on the rheology

Experimental results show that the frictional strength of serpentinite is considerably lower than that predicted by Byerlee's law, its coefficient of friction being 0.3–0.45 [62,63]. This result holds even if there is only 10% of serpentinisation [64]. We model this effect by changing the friction coefficient to 0.3 in Byerlee's law when serpentinite depletion is greater than 0.01. The effect of this decrease in friction coefficient is to further localise deformation in the area where serpentinisation occurs.

References

[1] J.W. Bown, R.S. White, Effect of finite extension rate on melt generation at rifted continental margins, J. Geophys. Res. 100 (1995) 18,011–18,029.

[2] G. Boillot, G. Féraud, M. Recq, J. Girardeau, "Undercrusting" by serpentinite beneath rifted margins: the examples of the west Galicia margin (Spain), Nature 341 (1989) 523–525.

[3] R.B. Whitmarsh, D.S. Sawyer, The ocean/continent transition beneath the Iberia Abyssal Plain and continental-rifting to seafloor-spreading processes, Proc. Ocean Drill. Program Sci. Results 149 (1996) 713–733.

[4] ODP Leg 173 Shipboard Scientific Party, Drilling reveals transition from continental breakup to early magmatic crust, EOS Trans., AGU 79 (1998) 180–181.

[5] G. Boillot, E. Winterer, Drilling on the Galicia margin: retrospect and prospect, Proc. Ocean Drill. Program Sci. Results 103 (1988) 809–828.

[6] I. Reid, Crustal structure of a nonvolcanic rifted margin east of Newfoundland, J. Geophys. Res. 99 (1994) 15,161–15,180.

[7] D. Chian, K. Louden, The ocean–continent crustal transition across the southwest Greenland margin, J. Geophys. Res. 99 (1994) 9117–9135.

[8] D. Chian, C. Keen, I. Reid, K. Louden, Evolution of non-volcanic rifted margins of the Labrador Sea, Geology 23 (1995) 589–592.

[9] D.M. Finlayson, C.D.N. Collins, I. Lukaszy, E.C. Chudyk, A transect across Australia's southern margin in the Otway basin region: crustal architecture and the nature of rifting from wide-angle seismic profiling, Tectonophys 288 (1999) 177–189.

[10] G. Manatschal, New models for evolution of magma poor rifted margins based on a review of data and concepts from the West Iberia and the Alps, Int. J. Earth Sci. (2004), doi:10.1007/00531-004-0394-7.

[11] I. Reid, H.R. Jackson, Oceanic spreading rate and crustal thickness, Mar. Geophys. Res. Lett. 14 (1987) 1238–1241.

[12] E. Klein, C.H. Langmuir, Global correlations of ocean ridge basalt chemistry with axial depth and crustal thickness, J. Geophys. Res. 92 (1987) 8089–8115.

[13] P.J. Michael, C.H. Langmuir, H.J.B. Dick, J.E. Snow, S.L. Goldstein, D.W. Graham, K. Lenhnert, G. Kurras, W. Jokat, R. Muehe, H.N. Edmonds, Magmatic and amagmatic seafloor

generation at the ultraslow-spreading Gakkel ridge, Arctic ocean, Nature 423 (2003) 956–961.
[14] F.M. Gradstein, F.P. Agterberg, J.G. Ogg, J. Hardenbol, P. van Veen, J. Thierry, Z. Huang, A Mesozoic time scale, J. Geophys. Res. 99 (1994) 24015–24074.
[15] R.B. Whitmarsh, G. Manatschal, T.A. Minshull, Evolution of magma-poor continental margins from rifting to sea-floor spreading, Nature 413 (2001) 150–154.
[16] G. Féraud, M.O. Beslier, G. Cornen, Ar–Ar dating of gabbros from the ocean–continent transition of the Western Iberia margin: preliminary results, in: R.B. Whitmarsh, D.S. Sawyer, A. Klaus, D.G. Masson (Eds.), Proceedings of the Ocean Drilling Program, Scientific Results, vol. 149, College Station, Texas, 1996, pp. 489–495.
[17] R.B. Whitmarsh, P.R. Miles, Models of the development of the West Iberia rifted continental margin at 40∞30′N deduced from surface deep-tow magnetic anomalies, J. Geophys. Res. (1995) 3789–3806.
[18] T.A. Minshull, S.M. Dean, R.S. White, R.B. Whitmarsh, Anomalous melt production after continental break-up in the southern Iberia Abyssal Plain, in non-volcanic rifting of continental margins: a comparison of evidence form land and sea, in: R.C.L. Wilson, R.B. Whitmarsh, B. Taylor, N. Froitzheim (Eds.), Geol. Soc. Spec., vol. 187, 2001.
[19] G. Bertotti, V. Picotti, D. Bernoulli, A. Castellarin, From rifting to drifting: tectonic evolution of the south-Alpine upper crust from the Triassic to Early Cretaceous, Sed. Geol. 86 (1993) 53–76.
[20] C. Chian, K.E. Louden, T.A. Minshull, R.B. Whitmarsh, Deep structure of the ocean–continent transition in the southern Iberia Abyssal Plain from seismic refraction profiles: Ocean Drilling Program (Legs 149 and 173) transect, J. Geophys. Res. 107 (1999) 7443–7462.
[21] C.M. Krawczyk, T.J. Reston, M.O. Beslier, G. Boillot, Evidence for detachment tectonics on the Iberia Abyssal Plain rifted margin, Proc. Ocean Drill. Program Sci. Results 149 (1996) 603–615.
[22] S.L.B. Pickup, R.B. Whitmarsh, C.M.R. Fowler, T.J. Reston, Insight into the nature of the ocean–continent transition from a deep multichannel seismic reflection profile, Geology 24 (1996) 1079–1082.
[23] S.M. Russell, R.B. Whitmarsh, Magmatism at the West Iberia non-volcanic rifted continental margin: evidence from analysis of magnetic anomalies, Geophys. J. Int. 154 (2003) 706–730.
[24] R. Hébert, K. Gueddari, M.R. Lafleche, Mo. Beslier, V. Gardien, Petrology and geochemistry of exhumed peridotites and gabbros at non-volcanic margins: ODP Leg 173, West Iberia ocean–continent transition zone, in: R.C. Wilson, R.B. Whitmarsh, B. Taylor, N. Froitzheim (Eds.), Non-volcanic Rifting of Continental Margins: Evidence form Land and Sea, Geol. Soc. (London) Spec. Publ., vol. 187, 2001, pp. 161–190.
[25] O. Muentener, T. Pettke, L. Desmurs, M. Meier, U. Schaltegger, Refertilization of mantle peridotite in embryonic ocean basins: trace element and Nd isotopic evidence and implications for crust–mantle relationships, Earth Planet. Sci. Lett. 221 (2004) 293–308.
[26] N. Abe, Petrochemistry of serpentinized peridotite form the Iberia Abyssal Plain (ODP Leg 173): its character intermediate between sub-oceanic and sub-continental upper mantle, in: R.C. Wilson, R.B. Whitmarsh, B. Taylor, N. Frotzheim (Eds.), Geol. Soc. London Special Publication: "Non-volcanic Rifting of Continental Margins: a Comparison of Evidence from Land and Sea", vol. 187, 2001, pp. 551–576.
[27] M. Pérez-Gussinyé, T.J. Reston, Rheological evolution during extension at nonvolcanic rifted margins: onset of serpentinisation and development of detachments leading to continental break-up, J. Geophys. Res. 106 (2001) 3961–3975.
[28] T.J. Reston, J. Pennel, A. Stubenrauch, I. Walker, M. Pérez-Gussinyé, Detachment faulting, mantle serpentinisation and serpentinite mud volcanism beneath the Porcupine basin, Southwest Ireland, Geology 29 (2001) 587–590.
[29] A.D.L. Skelton, J.W. Valley, The relative timing of serpentinisation and mantle exhumation at the ocean–continent transition, Iberia: constraints form oxygen isotopes, Earth Planet. Sci. Lett. 178 (2000) 327–338.
[30] J.N. Reddy, An Introduction to the Finite Element Method, McGraw-Hill, New York, 1984.
[31] P.K. Smolarkiewicz, A fully multidimensional positive definite advection transport algorithm with small implicit diffusion, J. Comput. Phys. 54 (1984) 325–362.
[32] K. Jha, M. Parmentier, J. Phipps Morgan, The role of mantle depletion and melt-retention buoyancy in spreading center segmentation, Earth Planet. Sci. Lett. 125 (1994) 221–234.
[33] Y. Chen, W.J. Morgan, A non-linear rheology model for mid-ocean ridge axis topography, J. Geophys. Res. 95 (1990) 17,583–17,604.
[34] J. Phipps Morgan, The Thermodynamics of Pressure-Release Melting of a Veined Plum-Pudding Mantle, G-cubed, 2, 2001-4-12 (electronic journal, 65 manuscript pages), 2001.
[35] J. Phipps Morgan, E.M. Parmentier, J. Lin, Mechanisms for the origin of mid-ocean ridge axial topography: implications for the thermal and mechanical structure at accreting plate boundaries, J. Geophys. Res. 92 (1987) 12,823–12,836.
[36] L. Ruepke, J. Phipps Morgan, M. Hort, J. Connolly, Serpentinite and the subduction zone water cycle, Earth Planet. Sci. Lett. 223 (2004) 17–34.
[37] O. Muentener, J. Hermann, V. Tromsdorff, Cooling history and exhumation of lower-crustal granulite and upper mantle (Malenco, eastern central Alps), J. Petrol. 41 (2001) 175–200.
[38] V. Gardien, G. Popeau, N. Muceku, R. Herbert, G. Beaudoin, E. Labrin, The evolution of amphibolites from Site 1067, ODP Leg 173 (Iberia Abyssal Plain): Jurassic rifting to the Pyrenean compression, in: R.C. Wilson, R.B. Whitmarsh, B. Taylor, N. Frotzheim (Eds.), Geol. Soc. London Special Publication: "Non-volcanic Rifting of Continental Margins: a Comparison of Evidence from Land and Sea", vol. 187, 2001, pp. 191–208.
[39] M. Pérez-Gussinyé, T.J. Reston, J. Phipps Morgan, Rheological and magmatic evolution of non-volcanic margins during progressive extension—the effect of initial lithospheric structure, in: R.C. Wilson, R.B. Whitmarsh, B. Taylor, N. Frotzheim (Eds.), Geol. Soc. London Special Publication: "Non-volcanic Rifting of Continental Margins: A Comparison of Evidence from Land and Sea", vol. 187, 2001, pp. 551–576.
[40] J.R. Hopper, T. Funck, B.E. Tucholke, H.C. Larsen, W.S. Holbrook, K.E. Louden, D. Shillington, H. Lau, Continental break-up and the onset of ultraslow seafloor spreading off Flemish Cap on the Newfoundland rifted margin, Geology 32 (2004) 93–96, doi:10.1130/G19694.1.
[41] B.E. Tucholke, R.B. Whitmarsh, The Newfoundland-Iberia conjugate rifted margins, in Principles of Phanerozoic Regional Geology, A.W. Bally and D.G. Roberts eds., in press.
[42] G. Piccardo, O. Muentener, A. Zanetti, T. Pettke, Ophiolitic peridotites of the alpine–apennine system: mantle processes and geodynamic relevance, Int. Geol. Rev. 46 (12) (December 2004) 1119–1159 (41).

[43] M. Cannat, How thick is the magmatic crust at slow spreading oceanic ridges? J. Geophys. Res. 101 (1996) 2847–2857.
[44] L. Desmurs, O. Muentener, G. Manatschal, Onset of magmatic accretion within a magma-poor passive margins: a case study from the Err-Platta ocean–continent transition, Eastern Switzerland, Contrib. Mineral. Petrol. 144 (2002) 365–382.
[45] O. Muentener, G.B. Picardo, Melt migration in ophiolitic peridotites: the message from the Alpine–Apennine peridotites and implications from embryonic ocean basins, in: Y. Kilek, P.T. Robinson (Eds.), Ophiolites in Earth History, Geol. Soc. London Spec. Publ., vol. 218, 2003, pp. 1–21.
[46] F.A. Frey, C.J. Suen, H.W. Stockman, The Ronda high temperature peridotite: geochemistry and petrogenesis, Geochim. Cosmochim. Acta 49 (1985) 2469–2491.
[47] C.J. Suen, F.A. Frey, Origins of the mafic and ultramafic rocks in the Ronda peridotite, Earth Planet. Sci. Lett. 85 (1987) 183–202.
[48] T.J. Reston, J. Phipps Morgan, Continental geotherm and the evolution of rifted margins, Geology 32 (2004) 133–136.
[49] E. Bonatti, M. Seyler, N. Sushevkaia, A cold suboceanic mantle belt at the Earth's equator, Science 261 (1993) 315–320.
[50] J.G. Schilling, C. Ruppel, A.N. Davis, B. McCully, S.A. Tighe, R.H. Kingsley, J. Lin, Thermal structure of the mantle beneath the equatorial Mid-Atlantic Ridge: inferences from the spatial variation of dredged basalt glass compositions, J. Geophys. Res. 100 (1995) 10057–10076.
[51] E.D. Bonatti, Brunelli, P. Fabretti, M. Ligi, R.A. Portaro, M. Seyler, Steady-state creation of crust-free lithosphere at cold spots in mid-ocean ridges, Geology 29 (2001) 979–982.
[52] J. Phipps Morgan, W.J. Morgan, Y.-S. Zhang, W.H.F. Smith, Observational hints for a plume-fed, suboceanic asthenosphere and its role in mantle convection, J. Geophys. Res. 100 (1995) 12,753–12,767.
[53] T.E. Tullis, F.G. Horowitz, J. Tullis, Flow-law of polyphase aggregates from end-member flow laws, J. Geophys. Res. 96 (1991) 8081–8096.
[54] G. Hirth, D.L. Kohlstedt, Experimental constraints on the dynamics of the partially molten upper mantle: 2. Deformation in the dislocation creep regime, J. Geophys. Res. 100 (1995) 15,441–15,449.
[55] J.D. Byerlee, Friction of rocks, Pure Appl. Geophys. 116 (1978) 615–626.
[56] Y. Gueguen, M. Darot, Les dislocations dans la fosterite deformée a haute temperature, Philos. Mag., A. 45 (1982) 419–442.
[57] S. Karato, P. Wu, Rheology of the upper mantle: a synthesis, Science 260 (1993) 771–778.
[58] P.C. Hess, Phase equilibria constraints on the origin of ocean floor basalts, in: J. Phipps Morgan, D. Blackman, J.M. Dinton (Eds.), Mantle Flow and Melt Generation at Mid-Ocean Ridges, American Geophysical Union, Washington D.C., 1992, pp. 67–102.
[59] A.H. MacDonald, W.S. Fyfe, Rate of serpentinisation in seafloor environments, Tectonophys 116 (1985) 123–135.
[60] D.S. O'Hanley, Serpentinites: Records of Tectonic and Petrological History, Oxford Monogr. Geol. Geophys., vol. 34, Oxford Univ. Press, New York, 1996 (277 pp).
[61] P. Ulmer, V. Trommsdorf, Serpentinite stability to mantle depths and subduction-related magmatism, Science 268 (1995) 858–861.
[62] J. Escartín, G. Hirth, B. Evans, Nondilatant brittle deformation of serpentinites: implications for Mohr–Coulomb theory and the strength of faults, J. Geophys. Res. 102 (1997) 2897–2913.
[63] J. Escartín, G. Hirth, B. Evans, Effects of serpentinisation on the lithospheric strength and the style of normal faulting at slow-spreading ridges, Earth Planet. Sci. Lett. 151 (1997) 181–189.
[64] J. Escartín, G. Hirth, B. Evans, Strength of slightly serpentinized peridotites: implications for the tectonics of oceanic lithosphere, Geology 29 (2001) 1023–1026.
[65] M. Fernandez, I. Marzan, A. Correia, E. Ramlho, Heat flow, heat production, and lithospheric thermal regime in the Iberian Peninsula, Tectonophys 291 (1998) 29–53.